Effect of Inflow Conditioning for Dry Powder Inhalers

Gajendra Singh[1], Albyn Lowe[1], Athiya Azeem[1], Shaokoon Cheng[2], Hak-Kim Chan[3], Ross Walenga[4], Agisilaos Kourmatzis[1, *]

1-School of Aerospace, Mechanical and Mechatronic Engineering, The University of Sydney, NSW 2006, Australia

2-School of Engineering, Macquarie University, NSW 2109, Australia

3-School of Pharmacy, The University of Sydney, NSW 2006, Australia

4-Division of Quantitative Methods and Modeling, Office of Research and Standards, Office of Generic Drugs, Center for Drug Evaluation and Research, US Food and Drug Administration, Silver Spring, MD, USA

Abstract

The transport of pharmaceutical dry powder inside an optically accessible inhaler-like device is studied using both macro- and microscopic high-speed imaging. The investigation aims to systematically study the effect of inflow modifications on the dispersion characteristics of agglomerates inside a dry powder inhaler (DPI) geometry. An inhaler device was designed with geometrical features akin to commercial inhalers used in the current market and research oriented inhalers such as the Twincer®: two offset inlet channels (one with a powder pocket), a clockwise swirling chamber and a single outlet channel. At the device outlet, a vacuum pump was fitted with an actuator and calibrated to achieve a steady state inhalation with a peak flowrate of 85 and 125 L/min. Airflow conditions at the intake of the device were strategically perturbed in order to induce powder fluidisation and dispersion using turbulence grids and through physically obstructing channel streams in order to achieve changes in flow behaviour (e.g., flow separation). Complete fluidisation of the powder bed was observed with image processing enabling statistics on de-agglomerated fragment size and velocity. A range of behaviour was noted including local turbulence through introduction of a grid, bimodal fragment size behaviour for cohesive mannitol powder, as well as introduction of low velocity zones in the device through flow splitting. The geometry enables simple

---

[1] School of Aerospace, Mechanical, and Mechatronic Engineering, The University of Sydney, Sydney, NSW, 2006, Australia

[2] School of Engineering, Macquarie University, Sydney, NSW, 2109, Australia

[3] School of Pharmacy, The University of Sydney, Sydney, NSW, 2006, Australia

Correspondence *agisilaos.kourmatzis@sydney.edu.au

systematic study of inflow conditions into a DPI-like device with the data being useful for study of a given powder formulation (mannitol) and validation of computational models.

1 Introduction

Commercially available dry powder inhalers (DPIs) demonstrate high variability in drug dispersion (approximately 12-40%) and fine particle fraction (approximately 9-78%) [1, 2, 3, 4]. Low variability in DPI performance is important for delivering predictable dosage and controlling the wastage of drug [1, 2, 5, 4]. In general, the device design, drug formulation, and inhalation characteristics are the main controlling parameters [6, 7, 8, 9, 10, 11]. Many available studies have used commercially available DPIs with a fixed design to shed light on the influence of the above parameters on DPI effectiveness [12, 13, 14, 15, 16, 17, 18]. **Recently, the effect of powder properties has been summarized by Mohammad et al. in their study of high dose delivery inhalers concerning tuberculosis treatment** [19]. Complementing these have been a number of more fundamental studies investigating de-agglomeration and fluidisation processes of DPI powders in more simplified geometries [1, 11, 20, 21, 22, 18]. What is, however, currently lacking in this space is a more systematic understanding of how certain key design features present in a DPI-like geometry influence subsequent fluidisation and de-agglomeration processes inside the device.

A systematic understanding of the effect of DPI design parameters on powder fluidisation and de-agglomeration characteristics in realistic geometries can be achieved through direct imaging and new image analysis methodologies [21]. Advanced imaging has been used recently where, while investigating fluidisation in a turbulence channel, it was reported that at lower Reynolds numbers (less than ~10,000), powder properties such as particle size and cohesion (as measured through the Carr's index)dominated the evacuation process [23]. The same group subsequently demonstrated the influence of a grid upstream of a powder pocket on the generation of localised turbulence, which expedites the evacuation process, even at a lower inhalation rates of 40 L/min [23, 24, 25]. The experiment, while insightful, was limited to a simplified channel flow [24]. In a recent study on the effect of grid on powder fluidisation using particle image velocimetry (PIV), Reis et al. [26] investigated the effect of the location of the grid inside the DPI. They concluded that the location of the grid has a significant impact on the powder dispersion and directly influences the particle deposition in the device and throat [26]. Advanced imaging tools have also been employed in the characterization of metered dose inhalers

(MDIs) [27, 28, 29], which is beyond the scope of this contribution, though a recent review provides a good coverage of recent advances in this area [21].

A critical parameter that controls powder fluidisation is the size of the air inlet, as this will partly dictate the local velocity and Reynolds number. Coates et al. [16], in their computational investigation of small air inlets, found that the DPI performance remains unaffected at low flow rates of the order of 35-45 L/min. However, at higher flow rates of 60 L/min, the performance was noted to deteriorate. Mehta et al. [10] confirmed this and reported that at 60 L/min, the wider inlets produce higher fine particle fraction values compared to small inlets. Both the studies were conducted using the Aerolizer® (Novartis Pharma AG, Basle, Switzerland) [16, 10], making the conclusions rather device-specific. Boer et al. [14, 12], in their study of the Twincer® (Indes, Enscede, Netherlands) inhaler, reported that the multiple air inlets and the flow split have a significant effect on powder fluidisation and should be considered in DPI design. The flow split is obtained using different geometries for air inlets to achieve different flow rates through them. Lee et al. [17] studied the effect of swirl, which can enhance fluidisation by increasing particle-wall collisions and particle-particle collisions [9, 17]. They reported that the angular momentum generated through swirl led to increased detachment of the drug agglomerates from their carriers resulting in more efficient dose delivery [17]. Alongside a higher likelihood of collisions, the swirl also helped achieve uniform fluidisation, thus reducing the effect of variable inhalation rate [9, 17]. Despite the growing research interest in DPI design parameters, most studies are limited to commercial DPIs, with each one having a slightly different geometric configuration, making it challenging to conclude which flow feature is most suitable for which powder.

Implementation of specific design features in DPIs can reduce the dependence of pulmonary drug delivery systems on patient characteristics [8, 30, 31, 3, 5, 4]. However, understanding the mechanisms to enhance de-agglomeration and fine powder dispersion within the inner geometry of DPIs is crucial, and for this to be developed, detailed quantitative characterisation of internal processes occurring in the device is critical. This paper investigates the particle-laden flow inside the mixing chamber of a swirling DPI-like device, where modification of the inflow into the device is achieved through air inlet modification and grid addition. The DPI-like device is designed in-house and allows

optical access for laser-based diagnostics. High-speed microscopic imaging is used to investigate key dispersion mechanisms. The research is motivated by two main objectives: (i) to develop an improved understanding of the evolution of pharmaceutical drug powders inside inhaler like flows and (ii) to understand the role of design modifications on powder dynamics, whilst in parallel producing a data set which can assist in the development of future computational models. **The reader should note that the focus in this manuscript is kept on studying the de-agglomeration process of highly cohesive (pure drug) agglomerate systems such that mainly larger fragments are produced. Dispersion of drug-carrier interactions are very important however it requires imaging of individual drug particles to a high degree of accuracy which is beyond the scope of this contribution. The structure of the paper is as follows.** The paper will first discuss the detailed experimental methodology and inhaler design. This will be followed by a brief overview of both macroscopic and microscopic imaging results. The paper will conclude with detailed statistical analysis of the evolution of powder dispersion for various inflow conditions including calculation of fragment size and velocity distributions inside the device.

2 Experimental Methodology

2.1 The Device

An optically accessible inhaler-like device, shown schematically in Figure 1a, was studied to isolate the effects of inflow conditions on the dispersion quality of pharmaceutical dry powders. **The flow channels of this device were designed for the purposes of flow visualization to investigate the de-agglomeration process; therefore, it is intended for research purposes only and not to be used as an actual DPI.** The overall layout of the geometry follows a similar design to that of the Twincer [14, 12] and has flat edges, making it easier to apply advanced diagnostics. The exploded view of the device in Figure 1b showcases the four primary components: the housing (top and base plate), the separator (mid-plate), the outflow (outlet adapter) and the inflow modifiers (slots and grids). The secondary components consist of a PTFE (Polytetrafluoroethylene) seal and seven fastening nylon nuts and bolts used to keep the device air-tight and leak-free. In Figure 1a top view, the housing, when combined, encloses the internal channels of the inhaler, and directs two inlet streams, labelled inlet "A" (air with pharmaceutical powder, 12 mm W x 5 mm H cross-section) and inlet "B" (air only, 12 mm W x 5 mm H cross-

section) into a swirl mixing chamber (16 mm radius). Inlet A has a 2 mm deep powder insert centred 14 mm from the inflow entrance and mimics the cross-section of typical "size 3" DPI gelatine capsules. Inlet A is intentionally offset from Inlet B by 4 mm to generate a clockwise swirl. The swirling particle-laden flow was directed from the mixing chamber to the outflow "C" by the separator through a 5 mm diameter hole, concentric to the swirling chamber. This means the swirling stream travels "out of the page" and takes a 90-degree bend before joining the outlet channel "C". The outflow C (5 mm W x 6 mm H cross-section) channel was connected to a vacuum pump which directly controls the steady-state inhalation applied over the acquisition time of the imaging setup, discussed in Section 2.3. The vacuum pump was fitted with a servo motor (HITEC HS7955TG) and ¼ inch ball valve to control the start and end of the inhalation, using a LabVIEW (National Instruments Corp., Austin, TX, USA) programme. The ball valve was connected to the lab air supply through a pressure gauge. The flowrates used were 125 L/min and 85 L/min. **These flowrates were used to ensure a fully turbulent flow and high enough inlet air velocity (comparable to typical DPIs) to fluidise the powders from the cavity effectively. Since the device dimensions (inlet cross-sections) are larger than a normal DPI, high flowrates are required to achieve velocity comparable to typical devices.** For each repetition of an experiment, first the desired pressure was set to achieve the required flowrate, next the drug was loaded (~40 mg) into the powder pocket of the inhaler device, and finally, the powder dispersion was achieved by a controlled inhalation using the LabVIEW programme which controls the servo-valve through an Arduino control board.

A key contribution of this work is the direct control of localised turbulence and swirl intensity while the inhalation and powder characteristics are maintained. This was achieved using inflow modifiers which are physical obstacles placed at the intake of the inhaler. Three inflow modes are studied here and labelled in Figure 1-C1 "Free" flow (no modifiers), 1-C2 "Grid" flow where a single grid is placed directly before the powder insert in Inlet A (dimensions: 6mm W x 3mm H x 1mm D with a 4 x 11 4mm diameter thru-hole pattern) and 1-C3 "Slot" flow, where a physical obstruction is applied to Inlet A, and its stream-lined cross-section is halved to 6 mm W x 5 mm H (using an inline slot). Apart from the inflow modifiers, the entire device was fabricated from Perspex® (Perspex International, Lancashire, United Kingdom) for optical access, while the slots

and grids were 3D printed with nylon (coloured red in Figure 1-C2 & C3) using a Markforged 3D printer.

Figure 1-C2 shows the two locations selected for high-speed imaging, indicated as Field-of-View A (FOVa) and Field-of-View b (FOVb). FOVa is situated downstream of the powder pocket and directly before the swirl chamber. This location facilitates imaging of the powder agglomerates flowing inside the channel immediately after their exit from the powder pocket. The second location FOVb, was chosen next to a wall inside the swirl chamber to visualise particle-wall interactions observed in high numbers at this location. At FOVa, the camera was focused at 4 mm from the inner bottom of the device. At FOVb, it was focused at 6 mm from the inner bottom. The location of the viewing plane was selected based on the maximum number of in-focus agglomerates observed at these locations. **It is expected that this shift in the plane containing maximum particles, at FOVb, may be caused by the upward velocity of particles exiting the device.**

2.2 Inflow Conditions and Powder Properties

Four dry powders are employed in this study: three spray-dried mannitol powders "M3", "M5" and "M7" with D50 = 2.92, 4.96 and 6.77 µm respectively and a lactose carrier SV010 (DFE Pharma), "C" with D50 = 106.1 µm. The mannitol powders are representative of active pharmaceutical ingredients (APIs) that exhibit agglomerating characteristics, while the lactose powder, SV010, does not form agglomerates. The size distributions of the spray-dried powders were determined on a wet disperser (Hydro SM, Malvern, Worcestershire, UK) connected to a laser diffractometer (Mastersizer 2000, Malvern, Worcestershire, UK). The refractive indices of mannitol used were 1.520 and 0.100 for the real and imaginary components, respectively, and the dispersing medium chloroform was 1.444. The population size distributions by volume for the four powders results in a cumulative volume diameter: D10|D50|D90 as follows. M3: 0.92|2.92|5.62 um, M5: 1.03|4.96|10.31 um, M7: 0.83|6.77|13.03, and SV010: 34.7|106.1|227.4. The halfwidth of these distributions is approximately 5 µm for all cases. **SV010 powder is employed for two purposes (i) to validate the image processing methodology discussed later in Section 2.4, and (ii) to decide the microscopic imaging location by observing the macroscale flow behaviour of SV010 inside the inhaler device. Since it does not de-agglomerate, it is not employed to study any quantitative microscopic behaviour.**

The reader should note that the agglomerate strength is lowest for M7 followed by M5 [22]. For M3, the agglomerate strength is highest among all the tested powders. For detailed powder properties, the reader is directed elsewhere [22].

Spherical mannitol particles were produced via a spray dryer (Buchi 290, Flawil, Switzerland) with an inlet air temperature of 140 °C, aspiration set at max 38 m^3/h and an atomising air rate of 800 NL/h (for full spray drying conditions, refer to [22]). The direct control of constituent particle population size was achieved by varying the feed concentration of raw mannitol in de-ionised water (>2 MΩm resistivity at 25 °C, obtained from the Modulab Type II Deionization System, Continental Water System) from 4 to 18 mg/mL and feed rate into the atomiser set to 3.8–8 mL/min.

The naming methodology of the experimental case studies is outlined in Table 1 such that the free-flow case M3-125 refers to a steady-state outflow profile with a peak flowrate of 125 L/min for a 40 mg mannitol powder loading with D50 = 2.92 μm (~3 micron, hence M3). The "grid" and "slot" inflow modes are denoted with a "G" and "S", respectively.

2.3 Imaging Setup

Microscopic backlit imaging (Figure 2) was conducted at a repetition rate of 7.2 kHz using a 300 W pulsed diode laser (Oxford Lasers Firefly) as an illumination source. The 808–810 nm beam is guided sequentially through a single 1" opal glass diffuser and a 2" collimating lens, which removes coherence from the beam and provides a uniform illumination source. After passing through the device, a 3" broadband dielectric mirror directs the light from a vertical to a horizontal plane. On the collection side, a high-speed complementary metal–oxide–semiconductor (CMOS) camera (Photron FASTCAM AX100, 16 GB) and long-distance microscope (Questar QM-100) are used to provide a field of view, field of view (FOV) (location in Figure 1-C2) of 4.81 mm W and 2.86 mm H with a 1024 × 608-pixel resolution; the images are collected for approximately 2.5 seconds for each inhalation repetition. At a 30.5 cm focal length, the QM100 lens results in a 47 μm depth-of-field centred on the mid-plane of the internal channel. The camera and laser are synchronized in frame-straddling mode, such that two laser pulses are positioned on sequential image frames. Each of the two exposures is recorded on separate frames, followed by analysis based on cross-correlation of the two frames.

To extract quantitative information from such images, they are binarized following a careful choice of pixel threshold. Binarization enables the identification of the interface between individual powder fragments and air. The uncertainties owing to the single pixel threshold used in this paper has been extensively studied in previous work that reported an error of 5-10 % in Sauter mean Diameter when compared with phase Doppler anemometry results [32, 33, 34, 35, 36, 22]. The image processing methodology adapted here limits the optical spatial resolution to 5.016 μm per pixel and a minimum measurable fragment size of approximately 21 μm. Therefore, in this contribution, the focus is on the **larger powder fragments formed through the de-agglomeration process instead of the analysis of fine particles that can erode from agglomerate surfaces**. **Such "larger" agglomerates are similar to those presented in** [22]**.** The velocity of the agglomerates is obtained by tracking them in subsequent images, using a particle tracking velocimetry (PTV) technique discussed elsewhere [36]. The uncertainty in velocity is limited to 10–15%. It is also important to understand that out-of-plane motion remains a limitation for single viewing angles. This can only be eliminated through the use of multi-angle imaging, which is outside the scope of this work. Similarly, a full consideration of impact de-agglomeration asymmetry due to the depth of field of the lens can only be fully accounted for by using multiple viewing angles. Notwithstanding these limitations, the calibration technique used here employed a binarization intensity threshold (with respect to the background) that varies from 50-60%, and this agrees well with recommended background thresholds used to binarize similar two-phase flow measurements in turbulent sprays for the same lens and camera layout [33, 32, 34, 35, 36].

For macroscopic imaging, a Nikon UV-NIKKOR 105mm f/4.5 telephoto lens is used in place of the micro lens used in microscopic imaging. The image size is 1024x608 pixels with a resolution of 70.6 μm/pixel. All the images are captured at 7200 Hz. These images are used to study the qualitative results discussed in section 3.

2.4 Uncertainties and Rejection

The narrow depth of field adapted in the high-speed microscopic imaging may lead to some error in object sizing due to (i) the artificial merging of out of focus objects and (ii)

the use of a single background threshold for binarization. The error associated with the size of the focused objects is quantified by visualising a calibration grid of 2 x 2 mm (Thor Labs) where an error of 0.017% in size is observed when the calibration grid is kept fully focused on the camera.

The error associated with out of focus objects is quantified by using images of SV010 carrier particles. These particles do not agglomerate and maintain an aerodynamic diameter of approximately 100 μm. The size distribution of these particles is compared for a range of background threshold from 25% to 75%. A 60% background threshold gives the best results with a mean particle size of 106 um. A similar binarization threshold was used in previous work which has shown physically consistent results [22, 33, 32, 34, 36, 35].

Therefore, for all the images, a 60% background threshold is used for image binarization with a lower limit of 4 pixels on the size of the objects is applied to avoid the error caused by noise.

3 Qualitative Results & Discussion

This section will discuss the general characteristics of the powder fluidisation in terms of the degree of dispersion, swirl, and residual powder deposition. Both macroscopic and microscopic imaging results are discussed. **The reader should note that the sampling time is kept similar for both macroscale and microscale images. However, only a few time instances are discussed for the microscale images in order to analyse the flow behaviour that cannot be resolved using macroscopic images.**

3.1 Macroscopic Imaging Observations

Representative snapshots of the global behaviour of dry powder dispersion with varying inflow conditions are shown in Figures 3 and 4. From top to bottom, the images represent a time instant after the start of inhalation (in ms) at 0 (start of inhalation), 5.56, 11.11, 16.67, 22.22, 125.97, and steady state (end of inhalation). Two parameters are explored in the instantaneous images; Figure 3 displays the effect of varying inflow conditions for

the M3 powder for the free flow, grid case, and slot case. Figure 4 shows the effect of powder composition for free flow cases of SV010 (carrier particles), M3, and M7.

In the images, the generation of clockwise-swirl is recognisable by 11.11 ms after initiation, depicted by a vortex of fine agglomerates populating the centre of the device mixing chamber. For all inflow modes, a dense shroud of fine agglomerates reaches the centre of the device before the larger agglomerates. The application of flow modifier in M3-S125 results in a denser shroud at the centre of the mixing chamber and the outlet stream when compared to the free flow case at t = 11.11 ms. A denser shroud is also observed for the grid case at 16.67 ms. This suggests that the flow modifiers promote dispersion, and the majority of large agglomerates change trajectory and fall into the central vortex. For the slot case M3-S125, at t = 11.11 & 16.67 ms, a second trail of dispersed powder appears alongside the main swirl (indicated by a box in Figure 3). This indicates the effect of the flow split, which is caused by a differential gas phase velocity across the air inlets (one of the air inlets has a smaller cross-section area). As a result of this separation in the flow, a region of low velocity develops near FOVb, resulting in the accumulation of large agglomerates (observed at 125.97 ms). This is better explained here through Figure 5, which shows instantaneous snapshots of the swirl chamber for case M3-S125 at an interval of 50 ms. Only a minor rotation of agglomerates with slow movement is observed in the images, confirming the existence of a low-velocity region in that area for the slot flow case.

On comparing the effect of powder composition (Figure 4), until 11.11 ms, the dispersion is similar for M3 and M7. After 11.11 ms, once the swirl develops, the dispersion is higher in the M7 cases compared to M3, observed at 16.67, and 22.22 ms in Figure 4. The reason for this is attributed to the lower agglomerate strength of M7 (less cohesive force among agglomerates) and a higher propensity for de-agglomeration compared to M3. Similar results for powder behaviour were observed by Lowe et al. [22] in their investigation of single agglomerate wall impaction. For SV010, due to the large size carrier particles, no significant swirl was noted. For all the studied cases, a significant amount of wall deposition is observed, confirmed here through images at the end of the inhalation (steady state) in Figures 3 and 4. **The dispersion behaviour of M5 falls in between M3 and M7, and it is difficult to find a clear demarcation between dispersion behaviour**

of all three powders using qualitative macroscale imaging only; therefore, the behaviour of M5 powder is investigated further using microscopic imaging.

3.2 High-Speed Microscopic Imaging

Figure 6 presents some representative instantaneous microscopic images of the inhalation process in the device at 28.33, 28.47 and 28.61 milliseconds after initiation (time progresses from top to bottom) at FOVb. Note that the "top" of the images in Figure 6 corresponds to the "left" of FOVb as defined in Figure 1. Only the FOVb images are discussed here, as at FOVa, the images for all the flow conditions look similar, except for the grid case M3-G125, where the flow is more dispersed compared to other cases. At FOVb, for the free-flow M3-125 and the slot case M3-S125, the majority of large agglomerates travel towards the inner swirl chamber wall towards the top of the image (indicated with an arrow). In contrast, when a grid is applied for M3-G125, the agglomerates generally move CW. This could be due to the slightly smaller agglomerate size observed in M3-G125 compared to M3-125 and M3-S125. Since the small agglomerates have more propensity to follow the flow, they are more likely to follow the direction of the swirl. This is more evident in the case of M7-125, where the large agglomerate is travelling straight towards the wall, whereas the trail of smaller agglomerates is moving in the CW direction (e.g., left to right as shown in Figure 6).

The agglomerates in M7-125 have a tail of smaller agglomerates arising due to shear driven de-agglomeration, confirming their lower agglomerate strength and higher propensity for de-agglomeration. Similar observations for M7 were reported by Lowe et al. [22] from their single agglomerate wall impaction investigation, extended here for inhaler like flows. This indicates that for softer agglomerates, de-agglomeration from both wall impaction and aerodynamic shear are important, whereas for stronger agglomerates (e.g., M3), impaction is a dominant mechanism. For the M7 powder, the dominance of impaction over shear or vice versa must be subject to further investigation. The microscopic image quality allows for spatially and temporally resolved size and velocity data, and this will be discussed in the following section.

4 Results & Discussion: Image Analysis

In this section, we first discuss the statistics of the area blocked by the powder (obscuration area) for location FOVa and FOVb. The next part will present and discuss the size and velocity population distributions.

4.1 Global Evolution of Powder Dispersion

Figure 7 presents the temporal evolution of the percentage blocked area for all the cases reported in Table-1 for location FOVa and FOVb. This is calculated as the ratio of the image area blocked by the powder agglomerates normalized by the total area of the image. Each plot shows the mean percentage blocked area (calculated using three repetitions); the error bars represent a 50% standard deviation. It is expected that the percentage blocked area is an indicator of the dispersed powder; thus, it is employed here to investigate the evacuation, dispersion, and flow behaviour of the powder. For all the cases, most of the powder exits the inhaler device within 0.25 s at 125 L/min; therefore, the data is presented up until that time instant.

$$Blocked\ Area\ (\%) = \frac{Number\ of\ pixels\ blocked\ by\ the\ powder}{Total\ number\ of\ pixels\ in\ the\ FOV} \times 100$$

4.1.1 FOVa

At FOVa and M3, initially, the trends for the blocked area are similar for all the flow conditions—the blocked area increases to approximately 65% for the free flow and slot cases and 45% for grid cases. The sudden flow of the powder causes a peak at the start of inhalation, suggesting a quick evacuation.

Comparing the grid cases only (comparing M3G125-top of Figure 7, M5G125-middle of Figure 7 and M7G125-bottom of Figure 7); initially, the rise in the blocked area is steep. The blocked area rises and falls steeply over a shorter duration of time for M3-G125 compared to the grid cases of M5 and M7. Since the M5 and M7 powders have less propensity for agglomeration than M3 [22], M5 and M7 disperse more readily, resulting in agglomerates from softer powders being more likely to be entrained closer to the powder pocket. After the peak, the trends are erratic for the grid cases, where the powder dispersion is prolonged due to the localised turbulence induced by the grid, however, it is clear that the M5 and M7 powders result in higher blocked areas due to the higher

degree of dispersion. Elserfy et al. [24, 25] reported a similar effect of erratic behaviour of powder fluidisation after a grid in their investigation of dispersion in a channel flow.

Both the free flow cases and the slot cases have similar flow behaviour at FOVa, suggesting a comparatively low impact of slot addition on powder evacuation. A higher blocked area is generally noted with the grid, which is caused by more wall deposition.

Of interest to note is also the variability in dispersion, presented here in the form of error bars (standard deviation/2), which is significantly higher for the M5 and M7 cases compared to the M3 powder. These two powders were consistently the least predictable in terms of their behaviour which leads to a more random deposition profile. This is most likely related to their lower strength, which leads to those powders de-agglomerating faster, leading to more erratic behaviour which can lead to variability in wall deposition and collision behaviour. Whilst this cannot be completely substantiated here, it is consistent with the observation of lower agglomerate sizes for M5 and M7 which is confirmed later in section 4.2.1.

4.1.2 FOVb

At FOVb in Figure 7, it is observed that the initial peak of the blocked area is smaller for the free flow M3-125 and slot case M3-S125 compared to the grid case. At this location, the particle flow is dominantly governed by swirl, and it is expected that only the smaller agglomerates which are more responsive to the flow will appear at this location. This suggests that the proportion of small agglomerates and powder dispersion is lower in these cases of M3 compared to the grid case. This is further substantiated by our earlier observation, in Section 3.2, where agglomerates were moving straight for M3-G125 and M3-S125 while moving in the CW swirl direction for the grid case M3-G125 (Figure 6). Comparing the free flow and the slot case, the rise in the blocked area is higher for M3-S125, which suggests that the overall higher gas phase velocity, induced by the reduced inlet cross-section area, slightly increases the dispersion in M3-S125, compared to the free flow case M3-125. The smaller peaks appearing in M3-S125 and M3-125, after the first peak, correspond to the larger agglomerates that appear later at this location.

The blocked area trends are most erratic for the slot case M3-S125, and the peaks are broader at FOVb. For this case, owing to the low-velocity region caused by the flow split, the agglomerates going past FOVb decelerate and take longer to leave the region, resulting in broader peaks in the blocked area. It is also observed that some of the agglomerates decelerate up to the point of near-zero movement (low-velocity zone mentioned in section 3) and do not evacuate within 0.25 s. This behaviour is not observed in any other case and is distinct in the slot cases.

For grid cases, the blocked area increases continuously to approximately 65% (for M3-G125) and 30% (for M5-G125); no decrease in area is observed past the peak. This can be attributed to the higher powder dispersion in grid cases driven by the localised turbulence generated through the grid. The small well-mixed agglomerates in the grid cases appear consistently in the swirl chamber, leading to a higher blocked area. A high wall deposition is also observed for all the grid cases leading to a high settling area observed here through Figure 7.

Comparing the effect of powder composition, it is observed that less cohesion between the agglomerates in the M5 and M7 cases result in higher powder dispersion and faster evacuation leading to a lower blocked area at FOVb for M5 and M7 compared to M3. For M7, the effect of flow conditioning is not observable at FOVb. The M7 powder disperses more than the other drugs, and so much of the powder evacuates the inhaler device without appearing at FOVb (i.e., it travels directly to the outlet).

4.2 Population Distributions

The flow conditioning effect on the powder dispersion is discussed here by presenting the size and velocity probability density functions (PDFs) for location FOVa and FOVb (Figures 8 and 9). The size and velocity are calculated by the in-house developed image processing technique mentioned in the methodology and discussed in detail elsewhere [36]. Each PDF is generated from the data obtained from three steady state inhalation repetitions of 2.5 seconds. For FOVa and FOVb, the average agglomerate size and velocity are presented in Table 2, for all the cases listed in Table 1. The size presented here is the average of the major and minor diameter of the objects, and the velocity is the resultant velocity of both velocity components.

4.2.1 Size

Figure 8 presents the PDF of the size of the agglomerates observed at FOVa and FOVb for all the cases tabulated in Table 1. First, we discuss the size PDF of the M3 cases, where for this particular powder, a bimodal size distribution is observed for all the flow conditions. The first peak occurs at ~30 μm, and the second peak is observed at ~90 μm—and it is more evident in the free flow case M3-125. Since M3 has a higher propensity for agglomeration, it is expected that some of the particles will form into larger agglomerates. This eventually leads to a bimodal size distribution with a peak at 80-100 μm, and a higher standard deviation in agglomerate size for M3-125 at FOVa, presented here in Table-2. On applying flow conditioning, the second peak shifts to a smaller size at ~60 μm due to higher dispersion caused by localised turbulence in the grid case and higher gas-phase velocity in the slot case. For the M5 and M7 cases, the powder dispersion is higher due to less cohesion amongst the agglomerates. Consequently, for M5 and M7, the overall size distribution is trending towards smaller agglomerates for all the cases, and the effect of flow conditioning is not as distinct as it is in the M3 cases. This is also reflected in the mean agglomerate size presented in Table 2, where the M5 and M7 cases have a smaller agglomerate size than the M3 cases at FOVa.

On observing the mean sizes presented in Table 2 for FOVb, it is found that the mean size is different for all three flow conditions, with grid cases having the smallest agglomerate size for M3 and M5. Owing to higher dispersion for the M7 cases, the mean agglomerate size is the lowest for M7 cases in each flow conditioning case. It is important to note that the standard deviation in agglomerate size is higher at FOVb compared to FOVa. This suggests that agglomerates of various size pass through this location which could be due to increased impaction as well as a larger influence of swirl, which generates shear-driven de-agglomeration (e.g., as observed for powder M7 in Figure 6).

At FOVb, Figure 8 shows that the grid cases have small-sized agglomerates with a peak at ~25 μm, and the major differences are observed in free flow and slot cases. For M3-S125, the size distribution is broad and has a bimodal distribution—one peak at ~40 μm and another at ~100 μm. The reason for this is not known and requires further investigation, however it may be related to a variation in the impaction characteristics at FOVb due to

the change in swirl behaviour when adding a slot, which is also evident from a high standard deviation for these cases, reported in Table-2.

In the M5 cases, the size distribution for M5-125 and M5-S125 is broad and shifted towards large-size objects compared to M5-G125. This is consistent with M3, in that the grid is able to better disperse the powder, however, the bimodality observed in M3-S125 is not observed in M5-S125 with a general shift towards larger sized agglomerates when compared to M3. This is initially unexpected given that at FOVa, it is clear that M3 exhibits the larger agglomerates (as it is the most cohesive powder). However, it is difficult to conclude the reasons behind larger agglomerates at FOVb, as there is a competing interaction of the powder properties and differing trajectories of differently sized agglomerates. For M5, much of the powder vacates before reaching FOVb (because it consists of smaller agglomerates at FOVa), and hence what is left in the imaging window at FOVb may be larger agglomerates which had higher inertia and hence did not escape the device; this does not necessarily imply that the M5 powder has larger agglomerates distributed throughout the flow.

The reader should note that, for reference, a discussion on the number density of the objects is presented in the Appendix.

4.2.2 Velocity

Figure 9 presents the PDF of the velocity of the agglomerates observed at FOVa and FOVb for all the cases tabulated in Table 1. At FOVa, the velocity distribution is similar for all the grid and free flow cases. However, for the slot cases, a bimodal velocity distribution is observed, showing a first peak at ~3 m/s and a second smaller peak at a high velocity of ~10-15 m/s. The bimodal distribution is more prominent in M3-S125 due to less dispersion of the M3 powder compared to M5 and M7. The higher velocity, corresponding to the second peak, for the slot cases compared to the grid and baseline case is expected as the air is travelling through a reduced cross section area (25% less) and hence has a higher velocity.

The effect of flow conditioning is more prominent at FOVb, shown in Figure 9 (right). For all three powders, the velocity distribution of the slot cases M3-S125, M5-S125, and M7-

S125 are very narrow and peak at a low velocity of ~1-2 m/s. This quantitatively confirms that, for the slot cases, some of the agglomerates decelerate up to the point of near zero velocity. It is also reflected through a very low average agglomerate-velocity for the slot cases at FOVb compared to other flow conditions, presented in Table-2. For the slot cases presented in Figure 9 (right), the smaller peaks appearing at higher velocities are due to some occasional faster moving smaller agglomerates, which did not manage to escape the device. The reader should note that, for reference, a discussion on the effect of flow rate is presented in the Appendix. This is not presented here for brevity, as the conclusions are consistent with the data presented so far.

5 Conclusion

The experiments presented have contributed towards improving understanding of the characteristics of dispersed pharmaceutical powders behaviour with different constituent particle sizes in an inhaler-like flow with different design configurations. A systematic study of the influence of key geometric features and powder properties has been presented using advanced high-speed imaging, demonstrating that simple changes to inflow conditions provide a degree of control over the behaviour of powders inside a DPI-like geometry. Specifically,

- The addition of a grid will make the dispersion process more erratic and can be effective at evacuating powders that are more cohesive, consistent with previous work [24].
- Changing the air inlet dimension in this device (slot addition) can lead to a flow split in the main swirl chamber which can alter the de-agglomeration process downstream. This is related to the creation of a near-zero velocity region in the flow (near FOVb) where agglomerates have low velocity.
- The less cohesive agglomerates of M5 and M7 are more prone to disperse and de-agglomerate faster compared to M3 agglomerates. However, these powders (M5 and M7) show a higher variability in their evacuation behaviour, as measured through their local blocked area, compared to the more agglomerated drugs (M3). As these powders are less cohesive, they fluidise faster and become more affected by the surrounding flow.

- A bimodal distribution of agglomerate size is noted for the M3 powders close to the powder pocket which dissipates downstream. This bimodality was not noted for other powders. The bimodality is also present in the velocity distribution (at higher velocities, particularly for the slot cases), though it is less pronounced.

- The distribution of agglomerate sizes close to the powder bed (Figure 8, FOVa) suggests that conditioning the flow through a grid or slot is likely to have a more significant influence on powders with more cohesiveness. Less cohesive powders disperse very rapidly, such that further de-agglomeration enhancing mechanisms have less of an overall effect.

Acknowledgments

References

[1] N. Islam and M. J. Cleary, "Developing an efficient and reliable dry powder inhaler for pulmonary drug delivery – A review for multidisciplinary researchers," *Medical Engineering & Physics,* vol. 34, pp. 409-427, 2012.

[2] N. Islam and E. Gladki, "Dry powder inhalers (DPIs)—A review of device reliability and innovation," *International Journal of Pharmaceutics,* vol. 360, pp. 1-11, 2008.

[3] J. A. Patil and S. Sarasija, "Pulmonary drug delivery strategies: A concise, systematic review," *Lung India : official organ of Indian Chest Society,* vol. 29, pp. 44-9, 2012.

[4] I. Sibum, P. Hagedoorn, A. H. de Boer, H. W. Frijlink and F. Grasmeijer, "Challenges for pulmonary delivery of high powder doses," *International Journal of Pharmaceutics,* vol. 548, pp. 325-336, 2018.

[5] M. Hoppentocht, P. Hagedoorn, H. W. Frijlink and A. H. de Boer, "Technological and practical challenges of dry powder inhalers and formulations," *Advanced Drug Delivery Reviews,* vol. 75, pp. 18-31, 2014.

[6] M. S. Coates, D. F. Fletcher, H.-K. Chan and J. A. Raper, "Effect of Design on the Performance of a Dry Powder Inhaler Using Computational Fluid Dynamics. Part 1: Grid Structure and Mouthpiece Length," *Journal of Pharmaceutical Sciences,* vol. 93, pp. 2863-2876, 2004.

[7] M. S. Coates, C. Hak-Kim, D. F. Fletcher and J. A. Raper, "Influence of Air Flow on the Performance of a Dry Powder Inhaler Using Computational and Experimental Analyses," *Pharmaceutical Research,* vol. 22, pp. 1445-53, 9 2005.

[8] W. H. Finlay, The Mechanics of Inhaled Pharmaceutical Aerosols, 2 ed., Academic Press, 2019.

[9] D. Harris, "The Advantages of Designing High-Resistance Swirl Chambers for Use in Dry-Powder Inhalers," *ON drugDelivery Magazine,* vol. 57, pp. 10-13, 2015.

[10] P. P. Mehta, S. S. Kadam and A. P. Pawar, "Influence of modified induction port, modified DUSA assembly and device air-inlet geometry on the aerosolization pattern of a dry powder inhaler," *Journal of Drug Delivery Science and Technology,* vol. 55, p. 101416, 2020.

[11] R. Tuley, J. Shrimpton, M. D. Jones, R. Price, M. Palmer and D. Prime, "Experimental observations of dry powder inhaler dose fluidisation," *International Journal of Pharmaceutics,* vol. 358, pp. 238-247, 2008.

[12] M. Hoppentocht, O. W. Akkerman, P. Hagedoorn, H. W. Frijlink and A. H. de Boer, "The Cyclops for pulmonary delivery of aminoglycosides; a new member of the Twincer™

family," *European Journal of Pharmaceutics and Biopharmaceutics,* vol. 90, pp. 8-15, 2015.

[13] C. Merusi, G. Brambilla, E. J. Long, G. K. Hargrave and H. K. Versteeg, "Optical diagnostics studies of air flow and powder fluidisation in Nexthaler®. Part II: Use of fluorescent imaging to characterise transient release of fines from a dry powder inhaler.," *Int J Pharm.,* Vols. 549(1-2), pp. 96-108, 10 2018.

[14] A. H. de Boer, P. Hagedoorn, R. Woolhouse and E. Wynn, "Computational fluid dynamics (CFD) assisted performance evaluation of the Twincer™ disposable high-dose dry powder inhaler," *Journal of Pharmacy and Pharmacology,* vol. 64, pp. 1316-1325, 2012.

[15] Q. T. Zhou, Z. Tong, P. Tang, M. Citterio, R. Yang and H.-K. Chan, "Effect of Device Design on the Aerosolization of a Carrier-Based Dry Powder Inhaler—a Case Study on Aerolizer® Foradile®," *AAPS Journal,* vol. 15, pp. 511-522, 4 2013.

[16] M. S. Coates, H.-K. Chan, D. F. Fletcher and J. A. Raper, "Effect of design on the performance of a dry powder inhaler using computational fluid dynamics. Part 2: Air inlet size," *Journal of Pharmaceutical Sciences,* vol. 95, pp. 1382-1392, 2006.

[17] H.-J. Lee, I.-H. Kwon, H.-G. Lee, Y.-B. Kwon, H.-M. Woo, S.-M. Cho, Y.-W. Choi, J. Chon, K. Kim, D.-W. Kim and C.-W. Park, "Spiral mouthpiece design in a dry powder inhaler to improve aerosolization," *International Journal of Pharmaceutics,* vol. 553, pp. 149-156, 2018.

[18] H.-K. Chan, "What is the role of particle morphology in pharmaceutical powder aerosols?," *Expert Opinion on Drug Delivery,* vol. 5, pp. 909-914, 2008.

[19] I. G. T. S. C. D. Mohammad A.M. Momin, "High dose dry powder inhalers to overcome the challenges of tuberculosis treatment," *International Journal of Pharmaceutics,* vol. 550, no. 1–2, pp. 398-417, 2018.

[20] A. Voss and W. H. Finlay, "Deagglomeration of dry powder pharmaceutical aerosols," *International Journal of Pharmaceutics,* vol. 248, pp. 39-50, 2002.

[21] A. Kourmatzis, S. Cheng and H.-K. Chan, "Airway geometry, airway flow, and particle measurement methods: implications on pulmonary drug delivery," *Expert Opinion on Drug Delivery,* vol. 15, pp. 271-282, 2018.

[22] A. Lowe, G. Singh, H.-K. Chan, A. R. Masri, S. Cheng and A. Kourmatzis, "Fragmentation dynamics of single agglomerate-to-wall impaction," *Powder Technology,* vol. 378, pp. 561-575, 2021.

[23] S. Mahmoudi, K. Elserfy, S. Cheng, H.-K. Chan, G. Hebbink and A. Kourmatzis, "Fluidisation characteristics of lactose powders in simple turbulent channel flows," *Experimental Thermal and Fluid Science,* vol. 103, pp. 201-213, 2019.

[24] K. Elserfy, A. Kourmatzis, H.-K. Chan, R. Walenga and S. Cheng, "Effect of an upstream grid on the fluidization of pharmaceutical carrier powders," *International Journal of Pharmaceutics,* vol. 578, p. 119079, 2020.

[25] K. Elserfy, S. Cheng, H.-K. Chan and A. Kourmatzis, "Local dynamics of pharmaceutical powder fluidization using high speed long distance microscopy and particle image velocimetry," *Experimental Thermal and Fluid Science,* vol. 124, p. 110367, 2021.

[26] L. G. dos Reis, V. Chaugule, D. F. Fletcher, P. M. Young, D. Traini and J. Soria, "In-vitro and particle image velocimetry studies of dry powder inhalers," *International Journal of Pharmaceutics,* vol. 592, p. 119966, 2021.

[27] Y. Chen, P. M. Young, S. Murphy, D. F. Fletcher, E. Long, D. Lewis, T. Church and D. Traini, "High-Speed Laser Image Analysis of Plume Angles for Pressurised Metered Dose Inhalers: The Effect of Nozzle Geometry," *AAPS PharmSciTech,* vol. 18, p. 782–789, 6 2016.

[28] C. A. DUNBAR, A. P. WATKINS and J. F. MILLER, "An Experimental Investigation of the Spray Issued from a pMDI Using Laser Diagnostic Techniques," *Journal of Aerosol Medicine,* vol. 10, pp. 351-368, 1997.

[29] H. Versteeg, G. Hargrave, B. J. Myatt, D. A. Lewis, T. Church and G. Brambilla, "Using phase Doppler anemometry & high speed imaging to analyze MDI spray plume dynamics," 2017.

[30] Y. Cui, S. Schmalfuß, S. Zellnitz, M. Sommerfeld and N. Urbanetz, "Towards the optimisation and adaptation of dry powder inhalers," *International Journal of Pharmaceutics,* vol. 470, pp. 120-132, 2014.

[31] C. Kleinstreuer, Z. Zhang and J. F. Donohue, "Targeted Drug-Aerosol Delivery in the Human Respiratory System," *Annual Review of Biomedical Engineering,* vol. 10, pp. 195-220, 2008.

[32] P. X. Pham, A. Kourmatzis and A. R. Masri, "Simultaneous volume-velocity measurements in the near field of atomizing sprays," *Measurement Science and Technology,* vol. 28, p. 115203, 10 2017.

[33] A. Kourmatzis, P. X. Pham and A. R. Masri, "A two-angle far-field microscope imaging technique for spray flows," *Measurement Science and Technology,* vol. 28, p. 035302, 1 2017.

[34] G. Singh, A. Kourmatzis and A. R. Masri, "Volume measurement of atomizing fragments using image slicing," *Experimental Thermal and Fluid Science,* vol. 115, p. 110102, 2020.

[35] Singh, Kourmatzis, Gutteridge and A. Masri, "Instability growth and fragment formation in air assisted atomization.," *Journal of Fluid Mechanics,* vol. 892, p. A29, 2020.

[36] G. Singh, A. Kourmatzis, A. Lowe, A. R. Masri, H.-K. Chan and S. Cheng, "Extending the range of back-lit imaging in two-phase flows using an interrogation-window based method," *Measurement,* vol. 176, p. 109155, 2021.

Appendix

A1) Number Density

Figure 10 shows the number density of the agglomerates for all the cases tabulated in Table 1 at FOVa and FOVb. Based on their size, the agglomerates are sub-ranged into six size bands (<25, 25-50, 50-75, 75-100, 100-125, and >125 μm). The number of agglomerates falling into each band is counted and normalised by the total number of images. Therefore, the numbers presented in Figure 10 shows the number of agglomerates of each size band that would have appeared in a single image (object/image).

At FOVa, the number density is similar for all flow conditioning, slot, grid and free flow for M3 powder. For M5 and M7, the number density is high for grid cases M5-G125 and M7-G125. This is due to the enhanced dispersion caused by the grid-induced local turbulence. It confirms our earlier observation in Section 4.1, where a higher blocked area was observed for these cases.

At FOVb, the effect of the grid is more prominent in the M3 cases than M5 and M7, reflected here through the higher number density for M3-G125 compared to M3-125 and M3-S125 in Figure 10. For M5 and M7, the number density is approximately similar for all the flow conditions, confirming our earlier discussion in Section 4.1 that the effect of flow conditioning is comparatively less significant for these powders. For all the cases, at FOVb, the number density of larger agglomerates (>125 μm) is higher for slot cases owing to the presence of large size agglomerates showing 'floating' like situation discussed earlier (shown in Figure 5).

A2) Effect of Flowrate

This section will focus on the effect of flowrate on powder fluidization. This is done here by comparing the blocked area and PDFs of size & velocity for two flow rates, 85 L/min and 125 L/min (Figure 11 & 12). Only the free flow condition, using M3 powder, is discussed in this section. Figure 11 shows the temporal evolution of the percentage blocked area at FOVa and FOVb for M3-85 and M3-125. Each plot shows the mean percentage blocked area (calculated using three repetitions).

At FOVa, it is evident that the peak blocked area is similar for both the flowrates, peaking at approximately 65%. However, the occurrence of the peak is slightly delayed for M3-85 compared to M3-125, which indicates that the lower flowrates progressively delay the powder evacuation. A similar but more distinct trend is observed at FOVb, where the occurrence of the peak is delayed by approximately 20 ms for M3-85 compared to M3-125. The settling blocked area is high at a higher flowrate of M3-125 at both FOVa and FOVb due to high wall deposition observed at this flowrate.

Figure 12(a) shows the number density of the agglomerates of a particular size band, sub-ranged into six size bands (<25, 25-50, 50-75, 75-100, 100-125, and >125 µm) at FOVa and FOVb. In general, at both locations, the number density is higher for M3-125 compared to M3-85, confirming a higher dispersion at high flow rates. The number density of large agglomerates (>125 µm) is higher for M3-85, indicating the presence of large unfragmented agglomerates. Figure 12(b) further confirms this by presenting the PDF of the particle sizes for both the flow rates. At FOVb, the probability of large size agglomerates is higher for M3-85. At FOVa, the particle size is slightly higher for M3-85; however, the bimodal size distribution for M3-85 is not as distinct as it is for M3-125. This could be due to the low flow rate in M3-85, which is insufficient to evacuate the large agglomerates resulting in low probability of large agglomerates at FOVa. This is also confirmed through Figure 12(a), where the number density of large agglomerates (75-125) is approximately zero for M3-85.

Figure 12(c) presents the velocity PDF for M3-85 and M3-125 for both locations. At FOVa, the PDFs are similar for M3-85 and M3-125, except that the peak velocity is slightly lower for M3-85 due to the low flowrate. The difference is more distinct at FOVb. For M3-125, the velocity distribution is bimodal, showing the first peak at ~2-3 m/s, which is similar to the peak velocity of M3-85. Unlike M3-85, a second smaller peak at ~12 m/s is observed for M3-125.

Table 1: Initial boundary conditions for mannitol (denoted by coefficient XX) agglomerates for "free" (XX-125 & XX-85), "grid" (XX-G125) and "slot" (XX-S125) inflow conditions. 'XX' represents the powder M3, M5, M7, and SV010. The velocity and Reynolds number are calculated for the combined inlet area of both the air inlets (Inlet A & P). The Reynolds number is calculated using the hydraulic diameter obtained from combined inlet area and perimeter of both the inlets.

Cases	XX-125	XX-G125	XX-S125	XX-85
Outlet Flowrate (g/min)	151	151	151	102
Outlet Velocity (m/s)	69	69	69	47
Outlet Reynolds No.	25275	25275	25275	17187
Inlet Velocity(m/s)	17.4	17.4	23.2	11.1
Inlet Reynolds No.	8294	8294	10071	5308

Table 2: Mean and standard deviation of size and velocity of agglomerates for all the cases listed in Table 1 for FOVa and FOVb. **These values are calculated from the data presented in Figure 8 & 9.**

|		M3-125	M3-G125	M3-S125	M5-125	M5-G125	M5-S125	M7-125	M7-G125	M7-S125
Size (um) FOVa	Mean	45.7	40.2	38.9	33.15	40.8	33.65	32.54	35.39	35.18
	Std	32.29	21.49	20.8	16.96	20.2	19.63	19.65	18.31	20.5
Size (um) FOVb	Mean	47.78	40.93	72.49	74.52	52.41	73.93	28.36	32.44	48.82
	Std	34.7	30.2	39.73	30.05	30.74	32.25	12.52	18.81	37.05
Velocity (m/s) FOVa	Mean	8.29	8.29	10.42	8.75	9.30	9.30	7.68	8.88	10.38
	Std	5.25	5.07	6.36	5.13	5.15	6.01	5.06	5.07	6.12
Velocity (m/s) FOVb	Mean	7.04	8.41	2.54	8.09	9.50	2.65	8.33	6.58	4.63
	Std	5.52	4.91	4.62	5.14	5.30	3.94	5.69	5.91	6.77
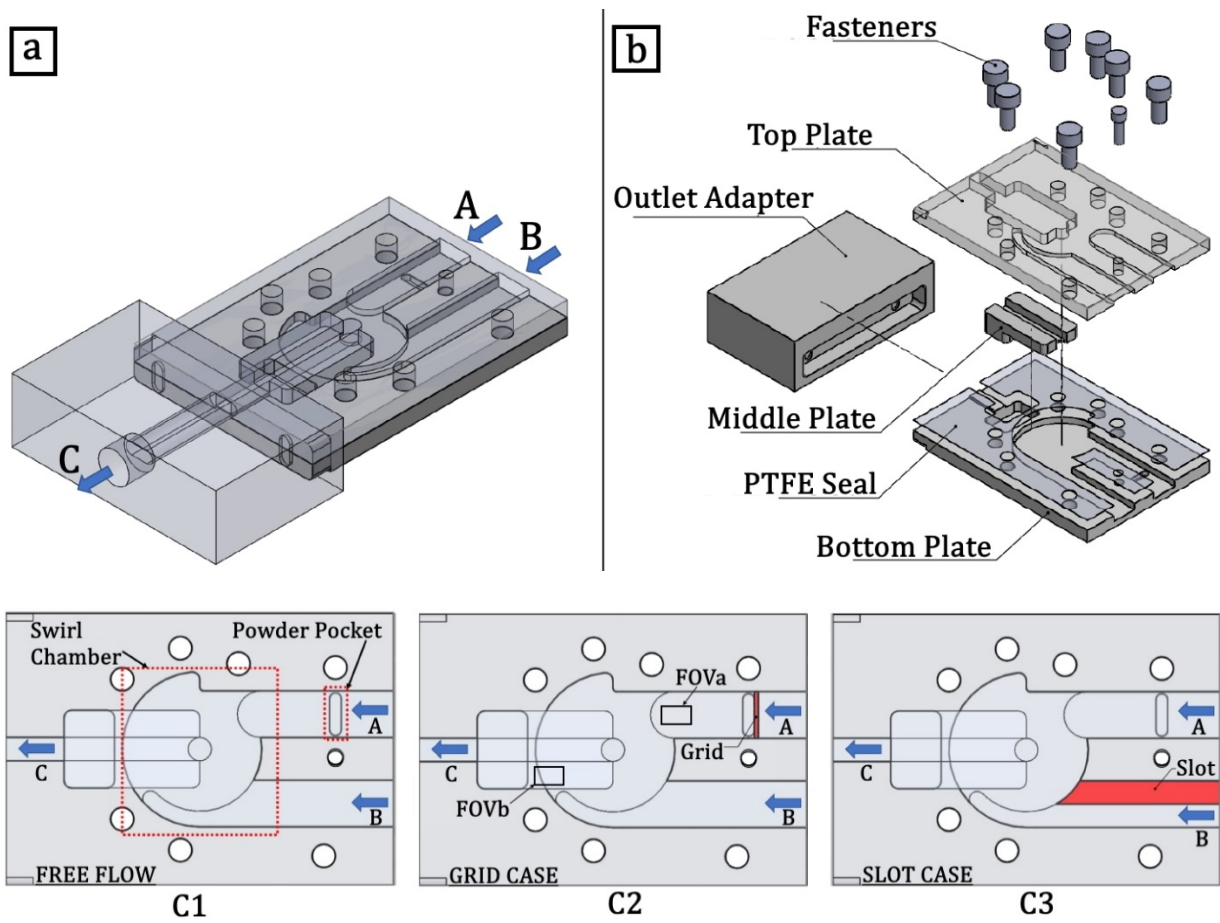
Figure 1 a) Assembled optical inhaler and b) Exploded view of optically DPI-like device. The bottom images show the three inflow modes, from left to right: Free flow, Grid case, and Slot case (respective inflow modifiers coloured red).
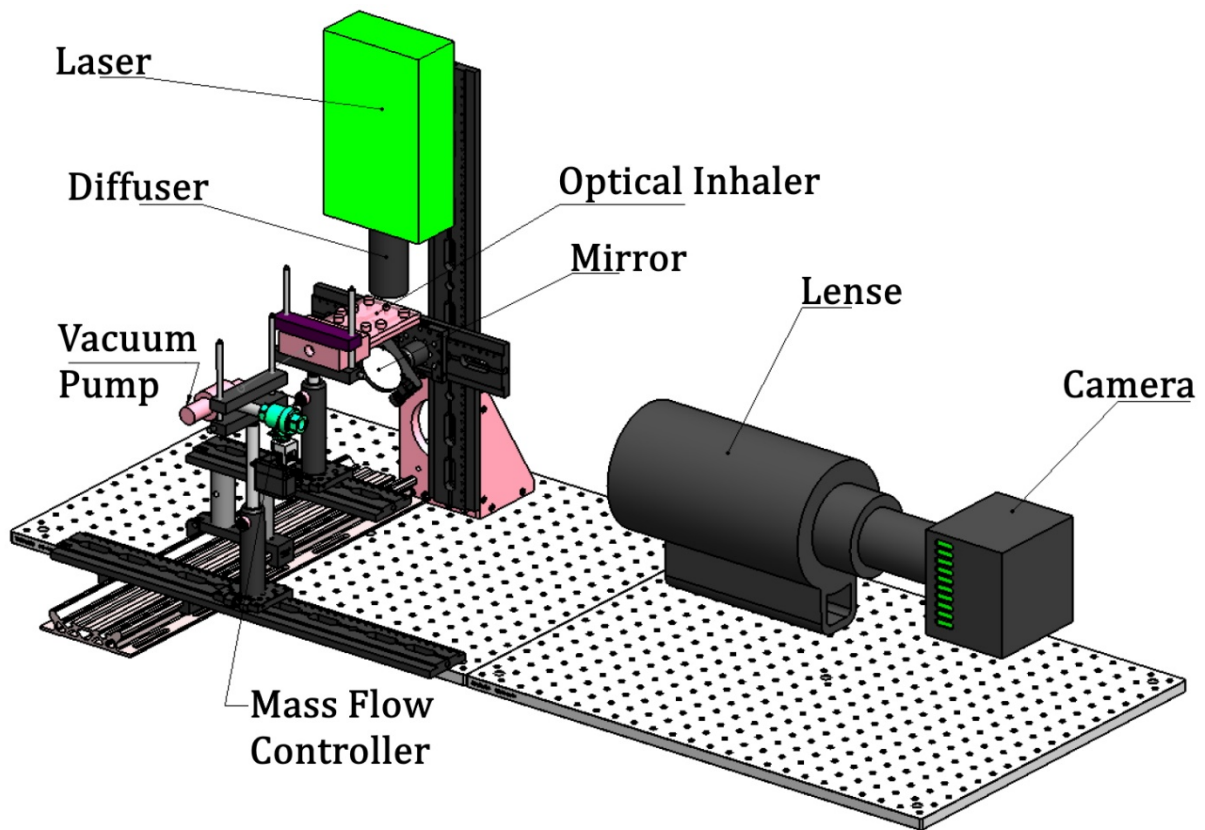
Figure 2 – High-speed microscopic backlit imaging setup with optically-accessible dry powder inhaler and vacuum pump for controlled inhalation.
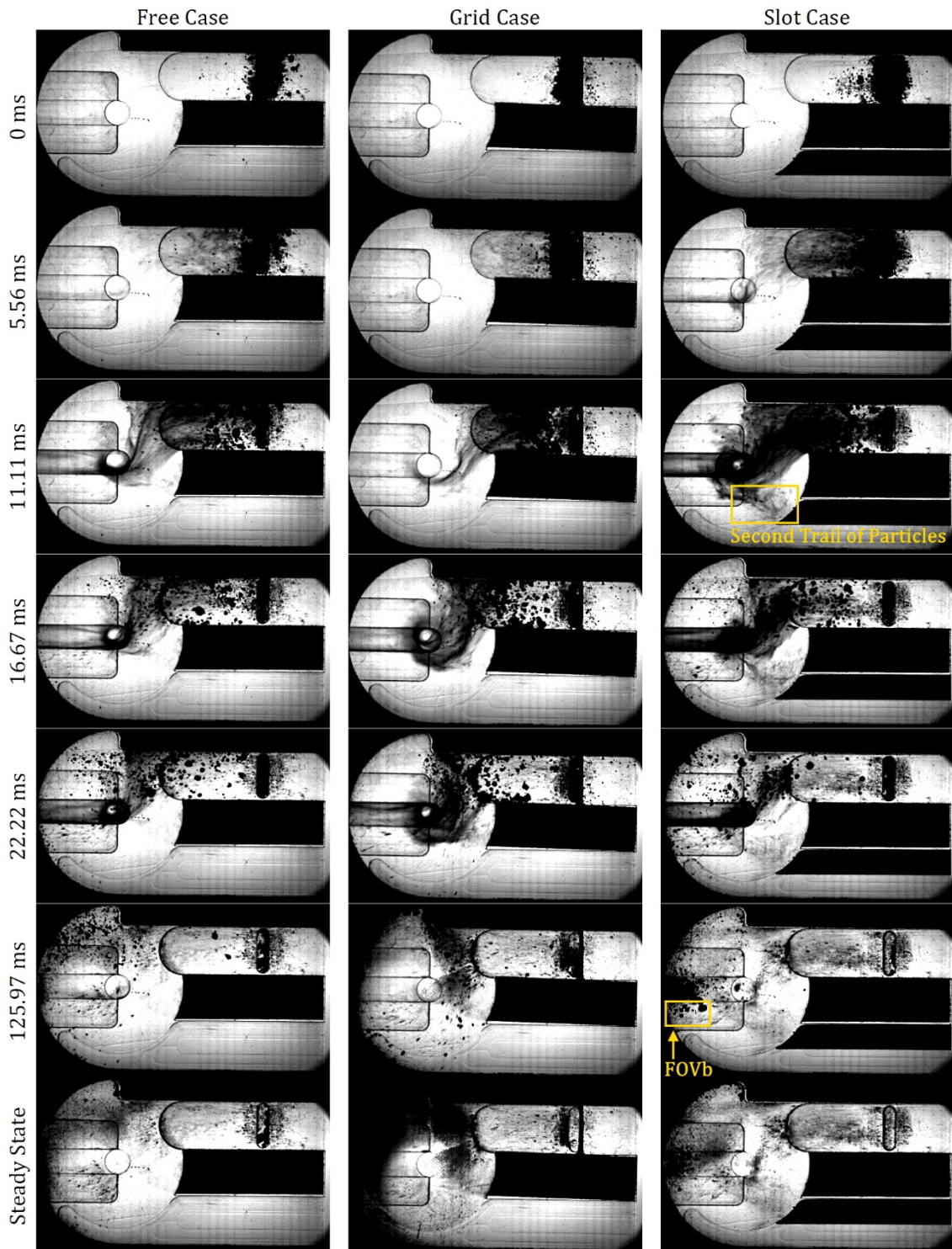
Figure 3 - Instantaneous high-speed macroscopic images of mannitol powder for varying inflow conditions of M3 powder, from left to right, free flow (M3-125), grid case (M3-G125), and slot case (M3-S125). From top to bottom the images represent a time instant (in ms) at 0 (start of inhalation cycle), 5.56, 11.11, 16.67, 22.22, 125.97, and steady state (end of inhalation cycle).
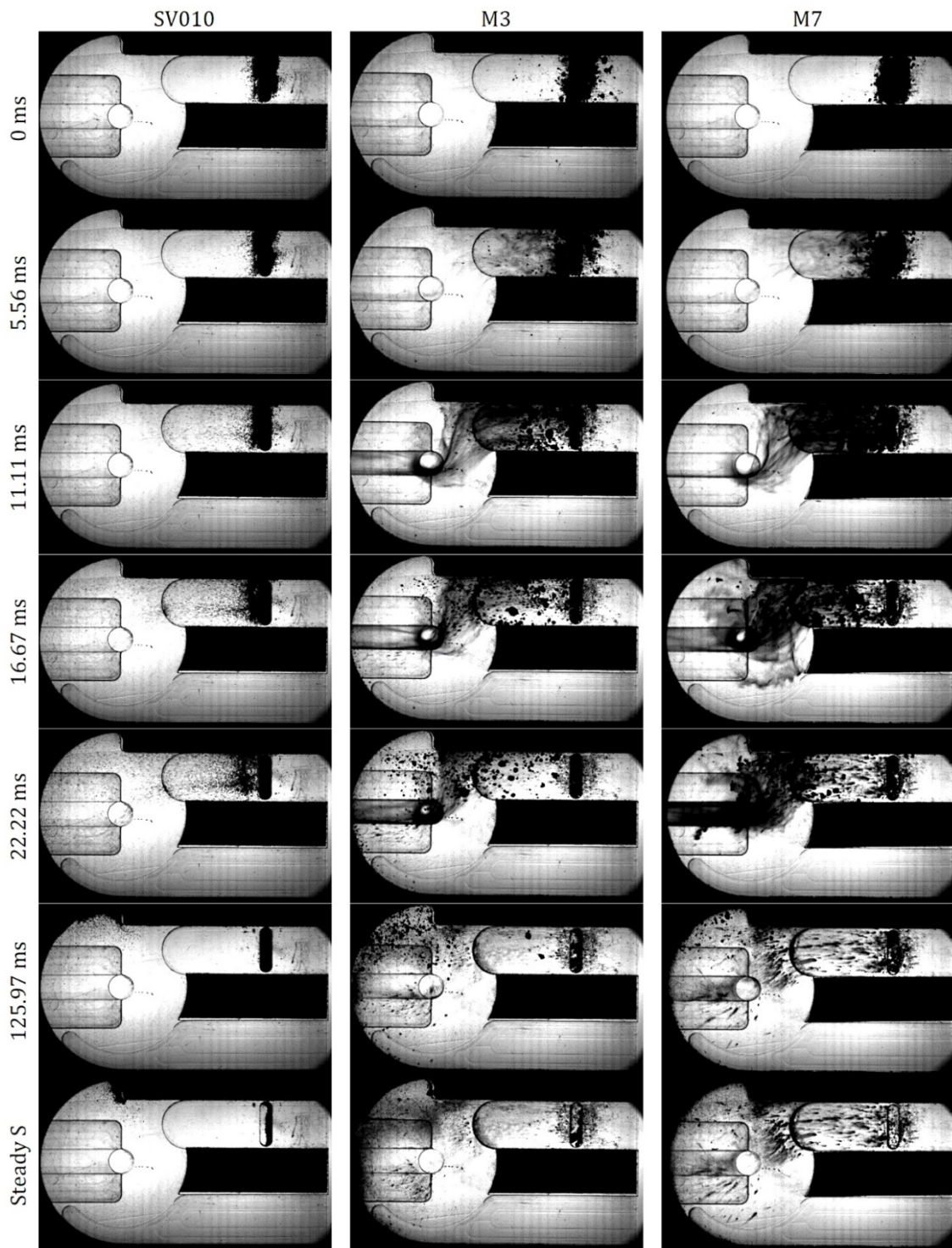
Figure 4 - Instantaneous high-speed macroscopic images of mannitol powder, for varying powder compositions for free inflow (constant 125 L/min outflow) from left to right SV010 (carrier agglomerates), M3-125, and M7-125. From top to bottom, the images represent a time instant (in ms) at 0 (start of inhalation cycle), 5.56, 11.11, 16.67, 22.22, 125.97, and steady state (end of inhalation cycle).
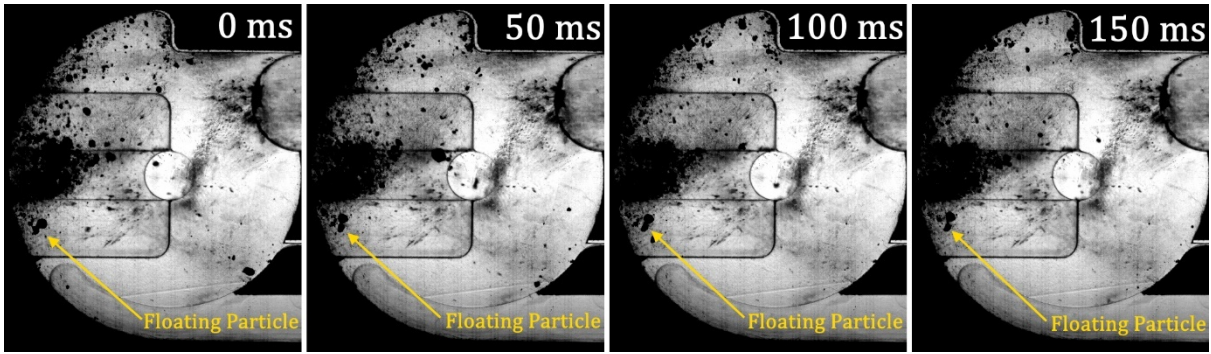
Figure 5: Instantaneous high-speed macroscopic images of mannitol powder, for case M3-S125. From left to right the images are at an interval of 50 ms. The images are showing the condition of 'floating' (low velocity zone) for some agglomerates at FOVb.
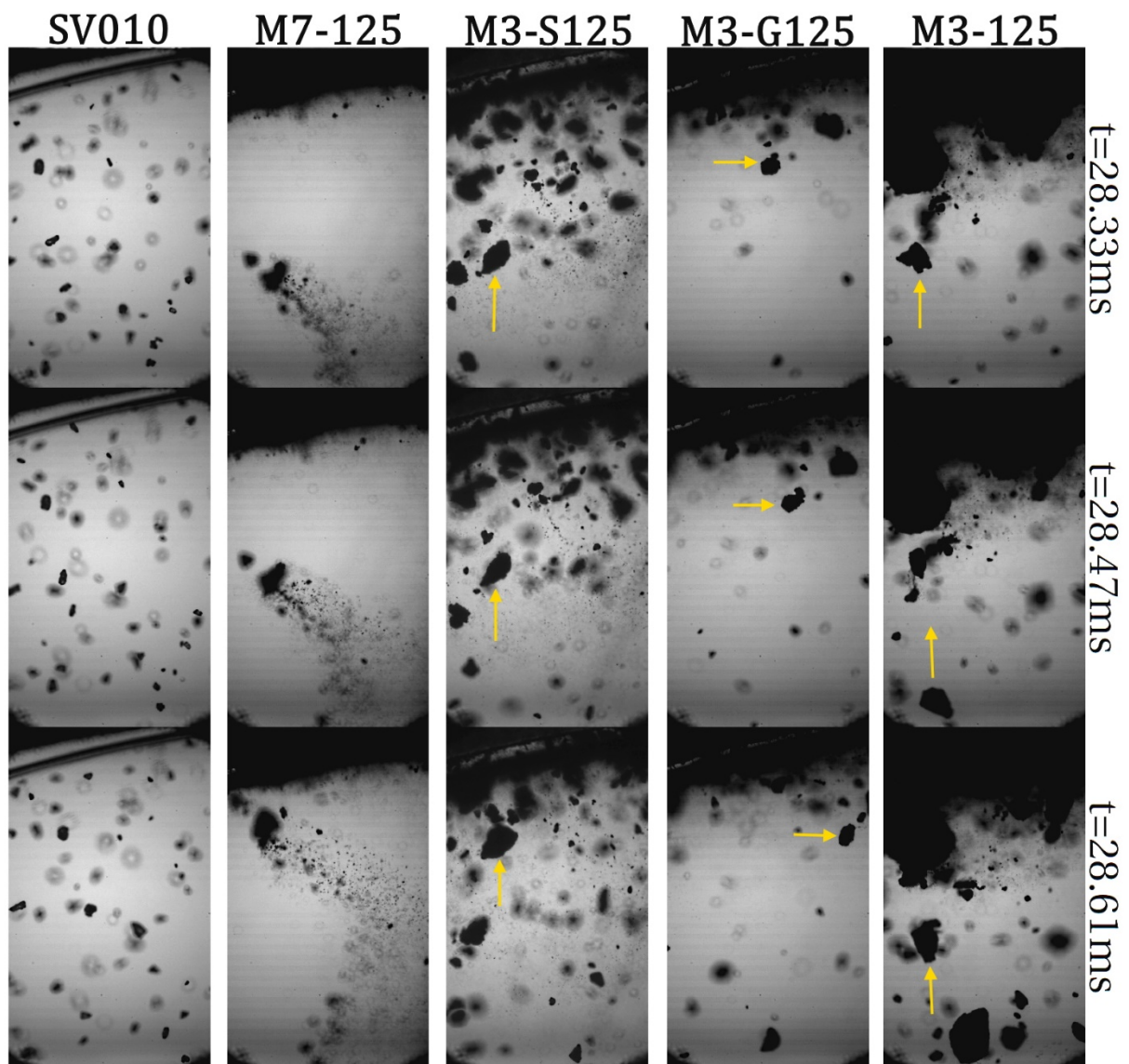
Figure 6 - Instantaneous high-speed microscopic images of suspended mannitol powder at FOVb as marked in Figure-3 (note: rotated 90deg clockwise); for varying inflow conditions of M3 powder, and varying powder compositions for free inflow (constant 125 L/min outflow). From left to right, SV010, M7-125, M3-S125, M3-G125, and M3-125. From top to bottom the images represent a time instant at 28.33, 28.47, 28.66 ms after start of inhalation.
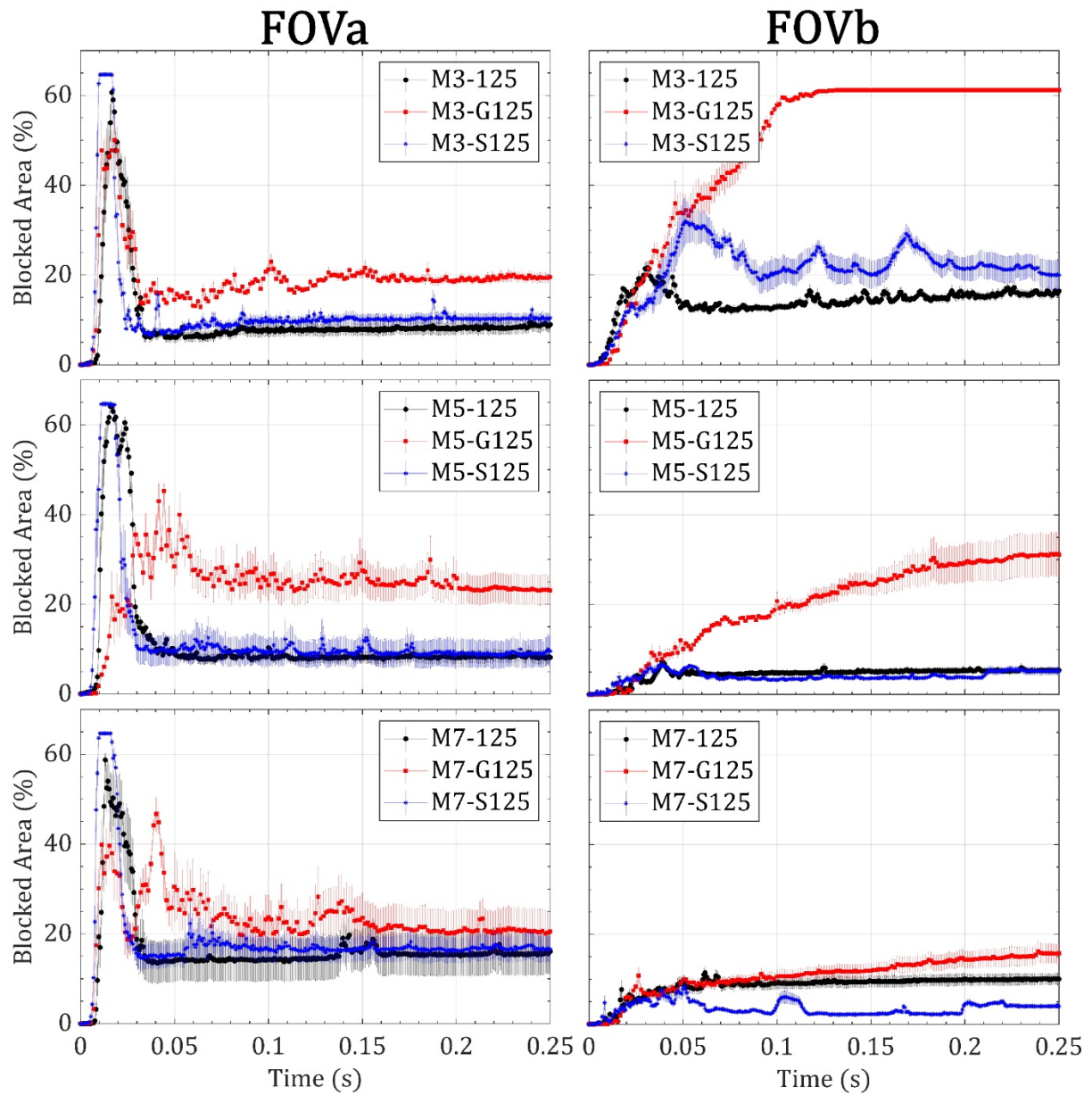
Figure 7 - Temporal evolution of percentage blocked area (fragment blocked area normalized by the acquisition FOV area per frame) for suspended mannitol powder at FOVa and FOVb for varying inflow conditions, free flow, grid case, and slot case, comparing mannitol powder compositions (top to bottom), M3, M5 and M7 respectively.
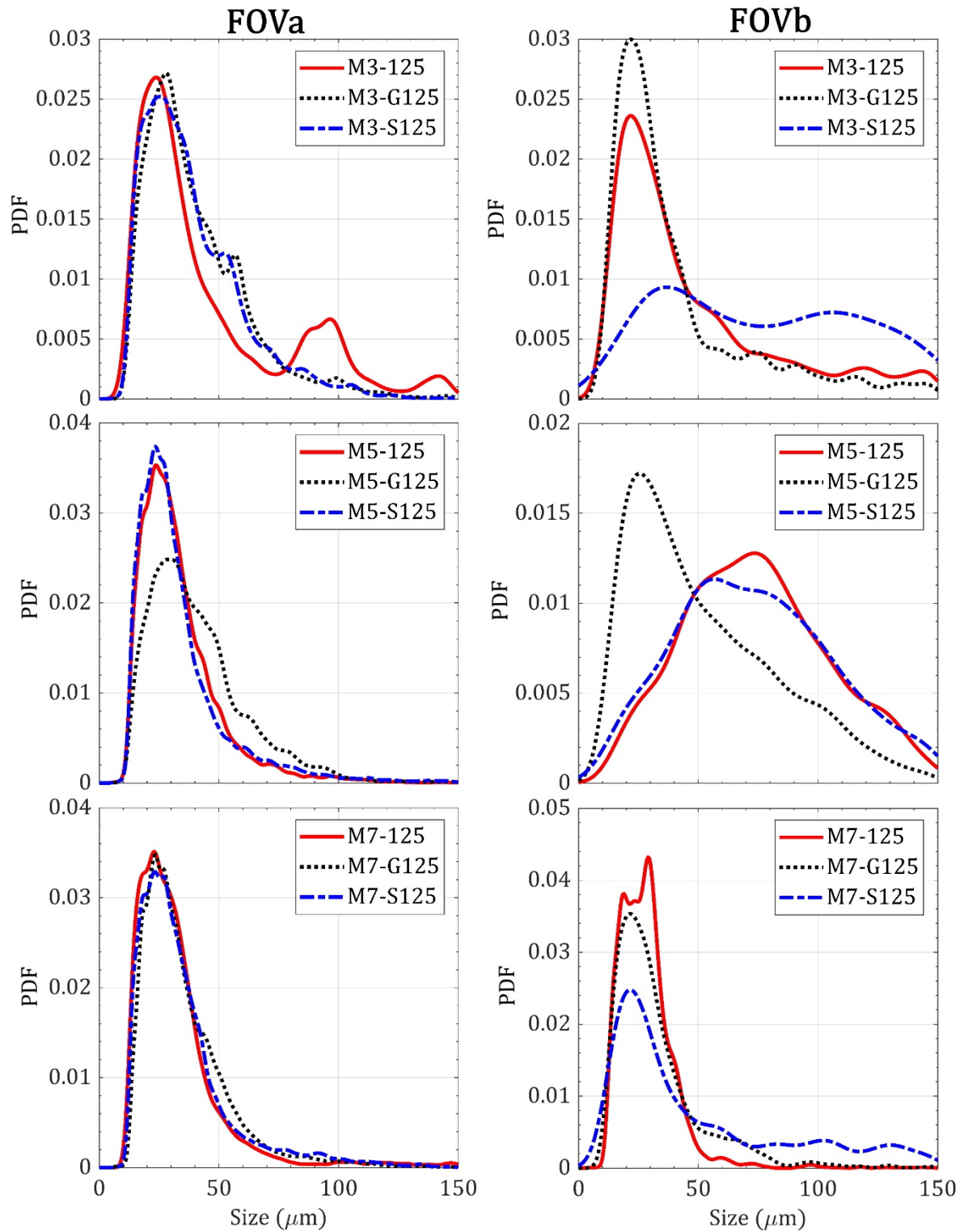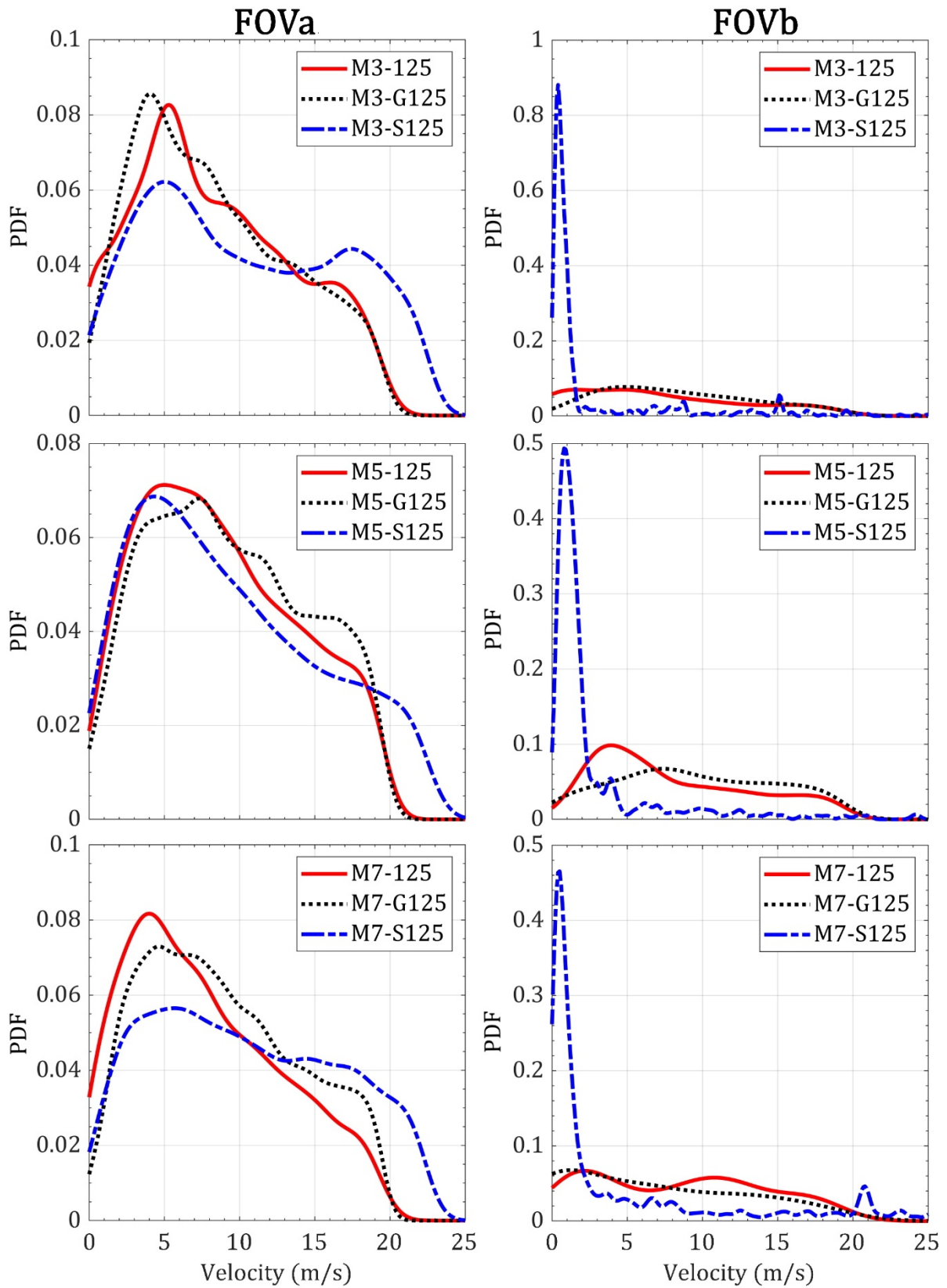
Figure 8 – Probability density function (PDF) of the particle size ($D_{maj}+D_{min}/2$) at FOVa and FOVb for mannitol powder with varying inflow conditions, free flow, grid case, and slot case; and varying powder composition (top to bottom), M3, M5, and M7 respectively.

Figure 9 – PDF of the particle velocity at FOVa and FOVb for mannitol powder with varying inflow conditions, free flow, grid case, and slot case; and varying powder composition (top to bottom), M3, M5, and M7 respectively.
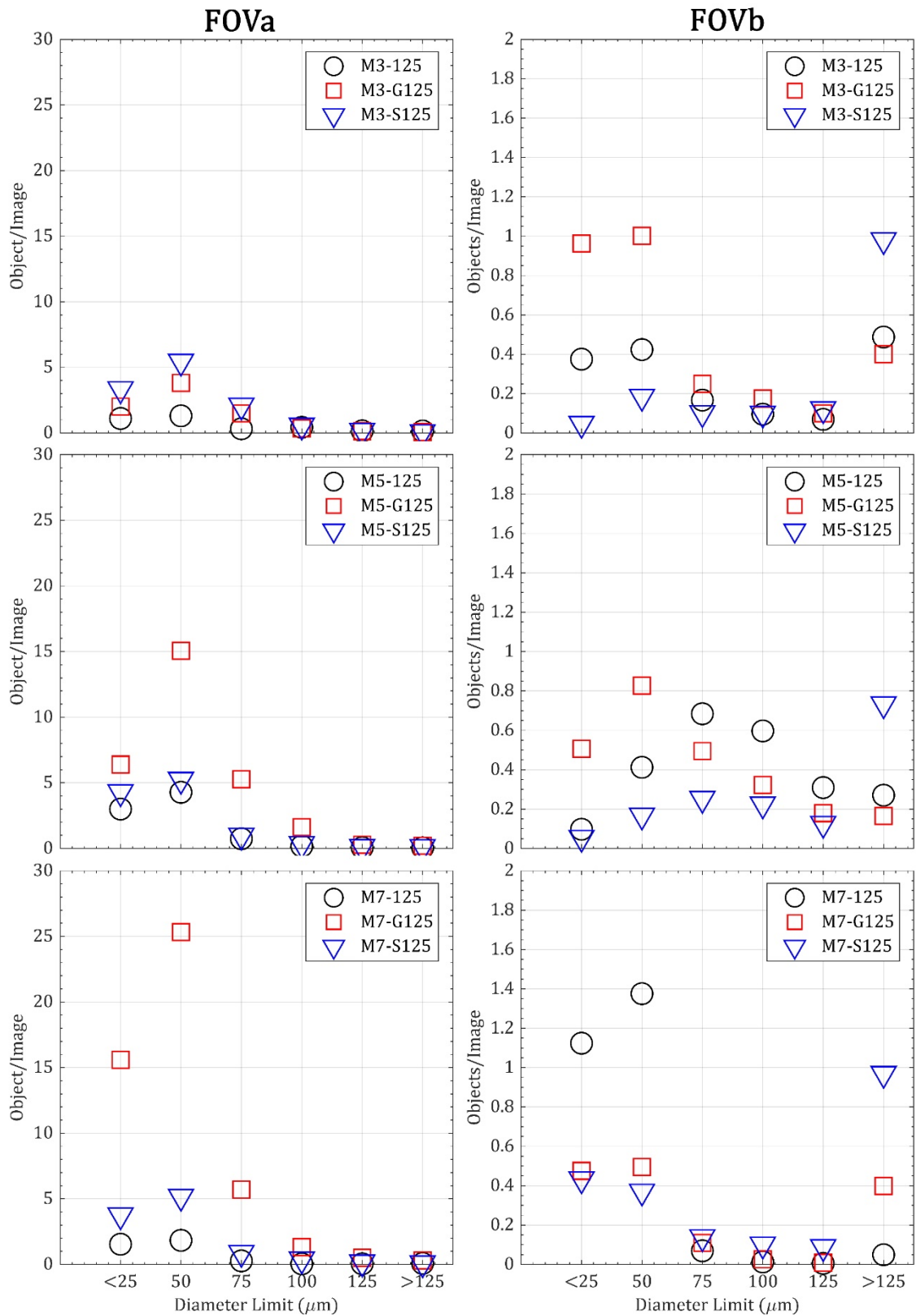
Figure 10 – Number of objects per image for various size ranges for mannitol powder at FOVa and FOVb for varying inflow conditions, free flow, grid case, and slot case; comparing mannitol powder compositions (top to bottom), M3, M5 and M7 respectively.
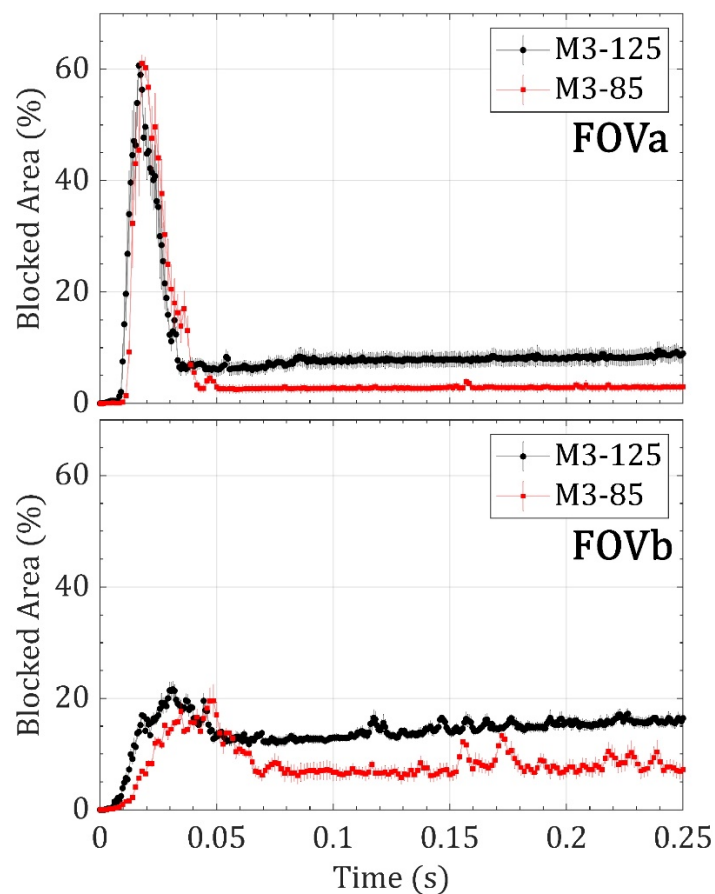
Figure 11 - Temporal evolution of percentage blocked area (fragment blocked area normalized by the acquisition FOV area per frame) for mannitol powder (M3) at FOVa and FOVb with varying flowrates of 85 L/min and 125 L/min in free flow condition.
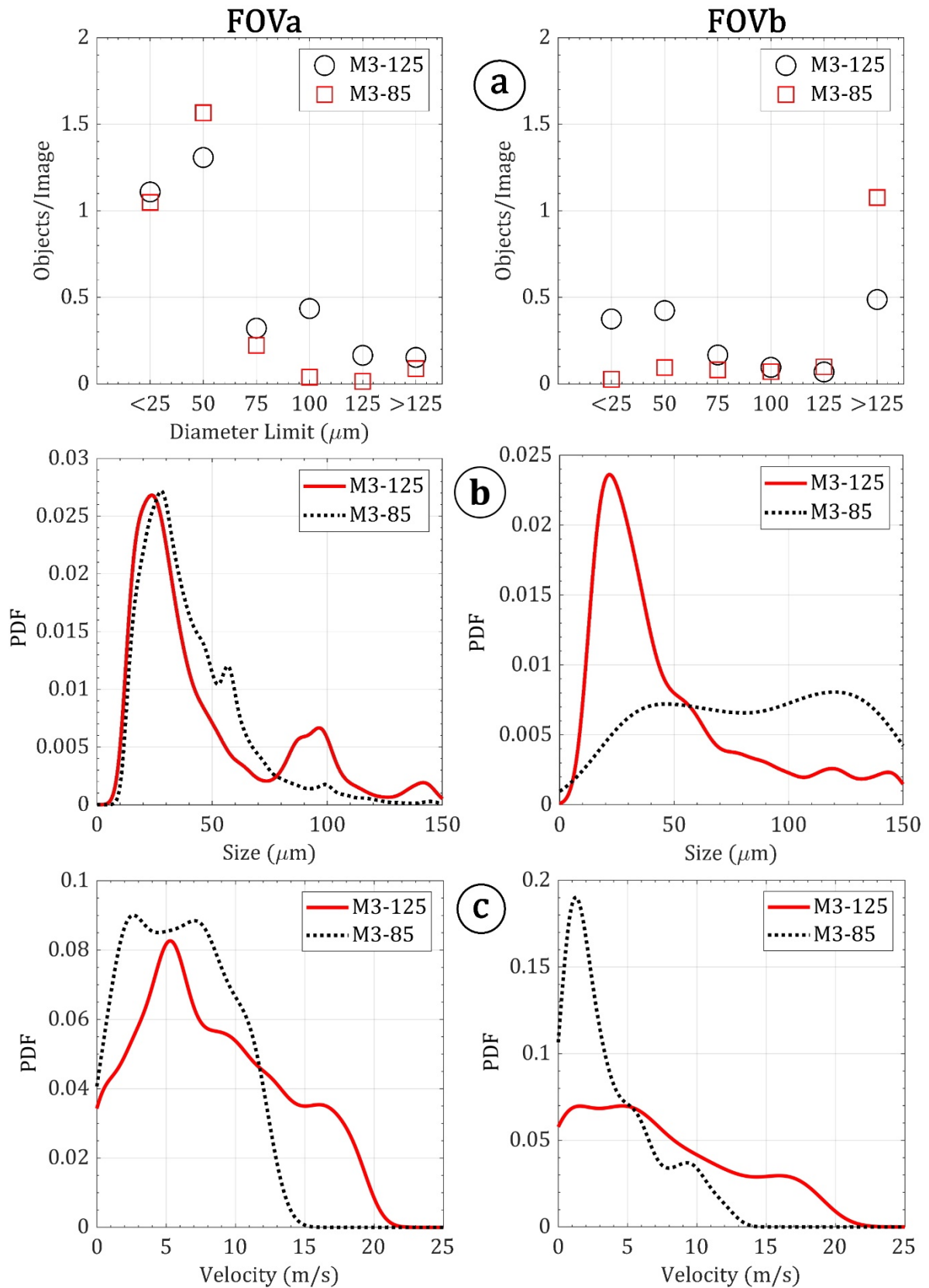
Figure 12 – The objects per image (a), PDF of size ($D_{maj}+D_{min}/2$) (b), and PDF of the particle velocity (c) at FOVa and FOVb for mannitol powder (M3) with varying flowrates of 85 L/min and 125 L/min in free flow condition.